Supplement of Geosci. Model Dev., 19, 5439–5490, 2026
https://doi.org/10.5194/gmd-19-5439-2026-supplement

Geoscientific Model Development
Open Access
EGU

Supplement of

Optimisation of ICON-CLM for the EURO-CORDEX domain: developments, sensitivities, tuning

Beate Geyer et al.

Correspondence to: Beate Geyer (beate.geyer@hereon.de)

General Information

Figures S2 to Fig. S20 showing seasonal means either as absolute values or differences between simulations or observations. Two different simulation periods are covered: 1980–1984 (simulation ID C2I***) and 2003–2008 (simulation IDs C2I***c).

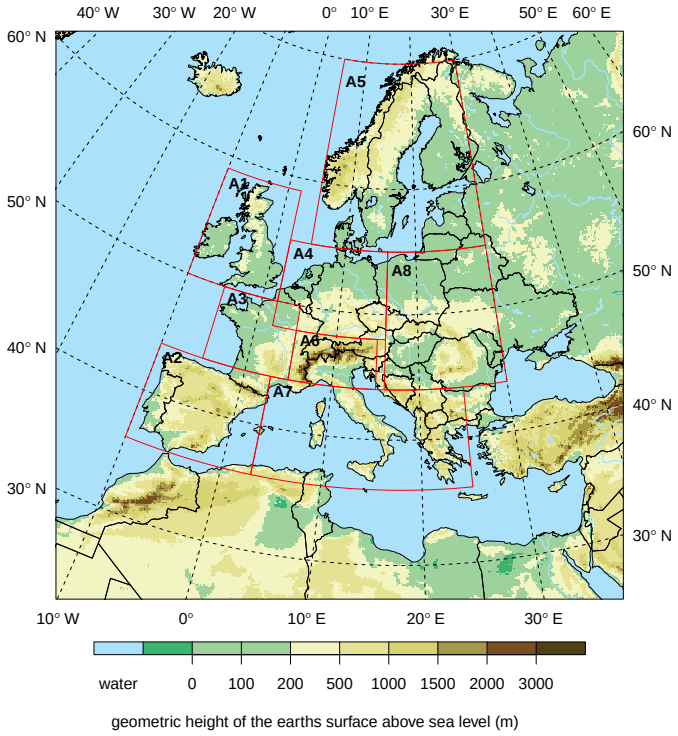

Figure S1. Simulation domain (EURO-CORDEX domain EUR-12) with its orography [m]. The different considered evaluation regions (known as PRUDENCE regions (Christensen and Christensen, 2007)) are marked in red: A1 British Islands; A2 Iberian Peninsula; A3 France; A4 Mid-Europe; A5 Scandinavia; A6 Alps; A7 Mediterranean; A8 East-Europe.

S1 Impact of external parameters

Soil Data (test: HWSDv2*, reference: FAO*)

Figure S2 shows seasonal mean differences exhibiting the impact of the difference in soil type distribution determined from HWSDv2 and FAO data for quantities given in the caption and additionally to those given in Fig. 4.

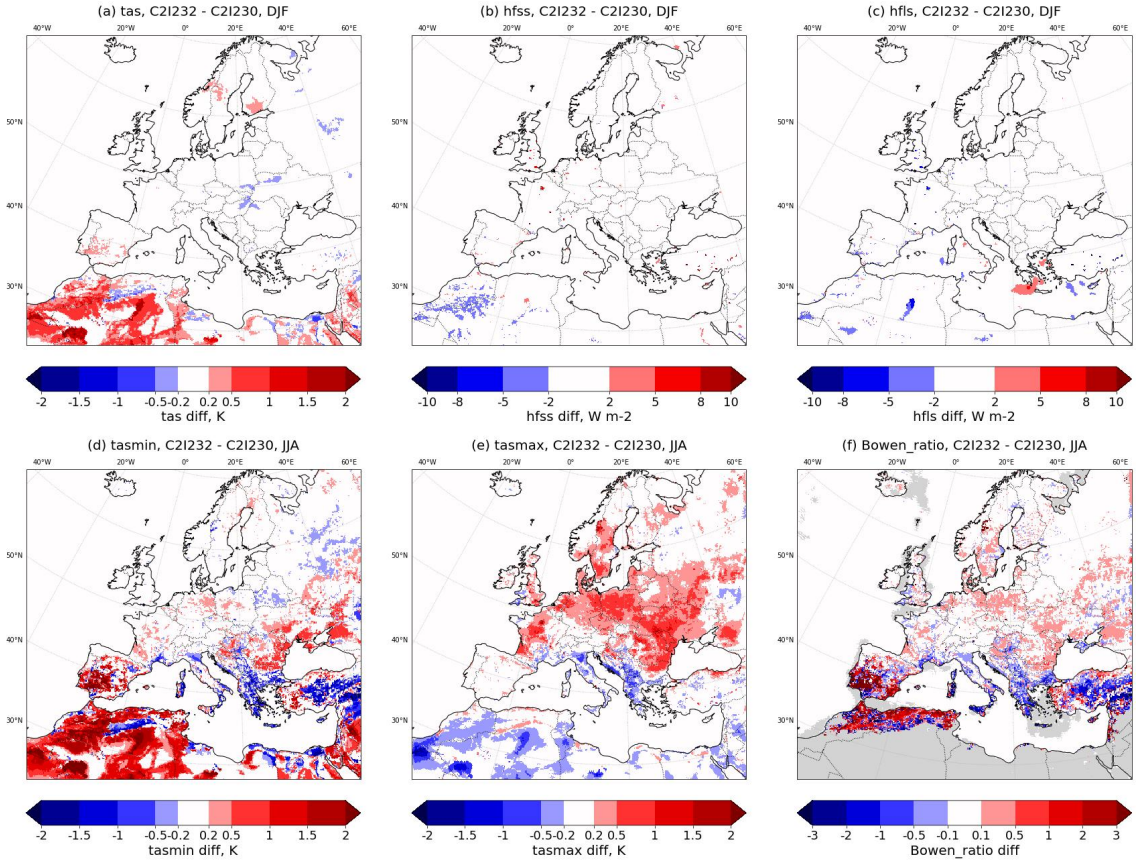

Figure S2. Sensitivity of ICON-CLM with respect to soil type distribution determined from `soil data HWSDv2` (test) and `FAO` (reference). Mean seasonal differences 2003–2008 between test and reference as defined in Table 6 in column 'signal' **tas** (a), sensible heat flux **hfss** (b) and latent heat flux **hfls** (c) in DJF and **tasmin** (d), **tasmax** (e), and Bowen ratio (f) in JJA.

Orography data and related model tuning (test: MERIT*, reference: GLOBE*)

Figure 6 shows seasonal mean differences for 10 m wind speed **sfcWind** exhibiting the impact of the difference in surface height determined from MERIT and GLOBE data together with tuning of model parameters for MERIT orography. Additionally, Fig. S3 shows the impact of changes in tuning parameter values (`C2I206-C2I246`) for MERIT orography and of MERIT vs. GLOBE data (`C2I246-C2I200`) separately. This exhibits that the tuning of the gravity wave and subgrid-scale orography scheme is resulting in a reduction of near-surface wind due to increased damping.

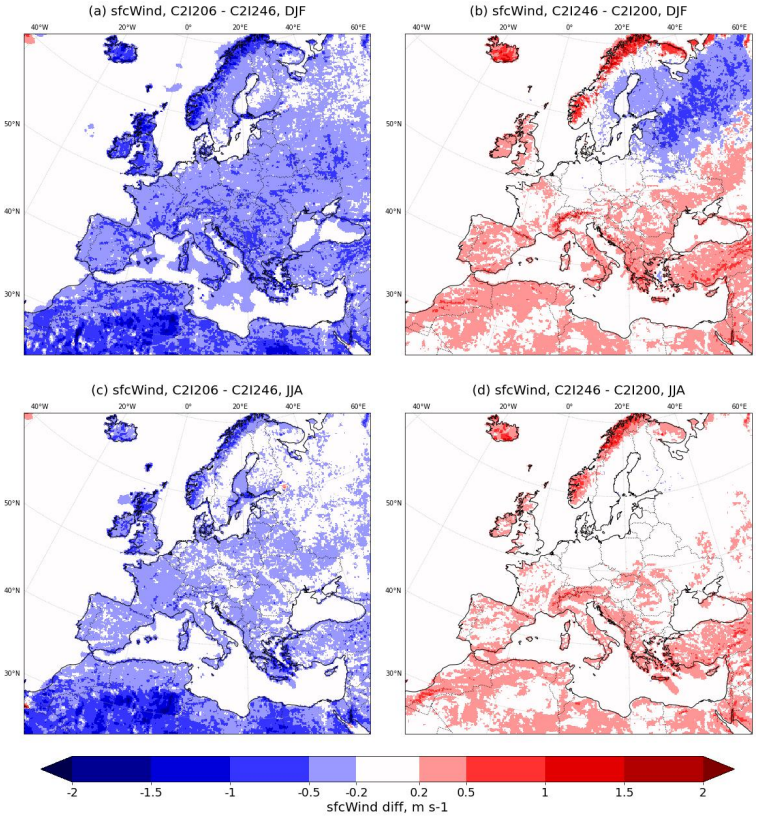

Figure S3. Sensitivity of ICON-CLM with respect to `orography` data MERIT (`C2I246`) vs. GLOBE (`C2I200`) and vs. additional tuning of gravity wave and subgrid scale orography scheme (`C2I206`). We show differences of **sfcWind** for DJF (top) and JJA (bottom) for 2003–2008 and tuning only (`C2I206-C2I246`, left: a and c) and orography data only (`C2I246-C2I200`, right: b and d).

Natural and anthropogenic transient Aerosol `irad_aero` (test: MACv2-SP*, reference: Tegen*)

Figure 7 shows seasonal mean differences for **rsds**, **tasmin** and **tasmax** in JJA exhibiting the impact of the difference in Aerosol concentration in 1980–1984. Additionally, Fig. S4 shows the mean difference in Aerosol Optical Depth and in downward longwave radiation at the surface **rlds**.

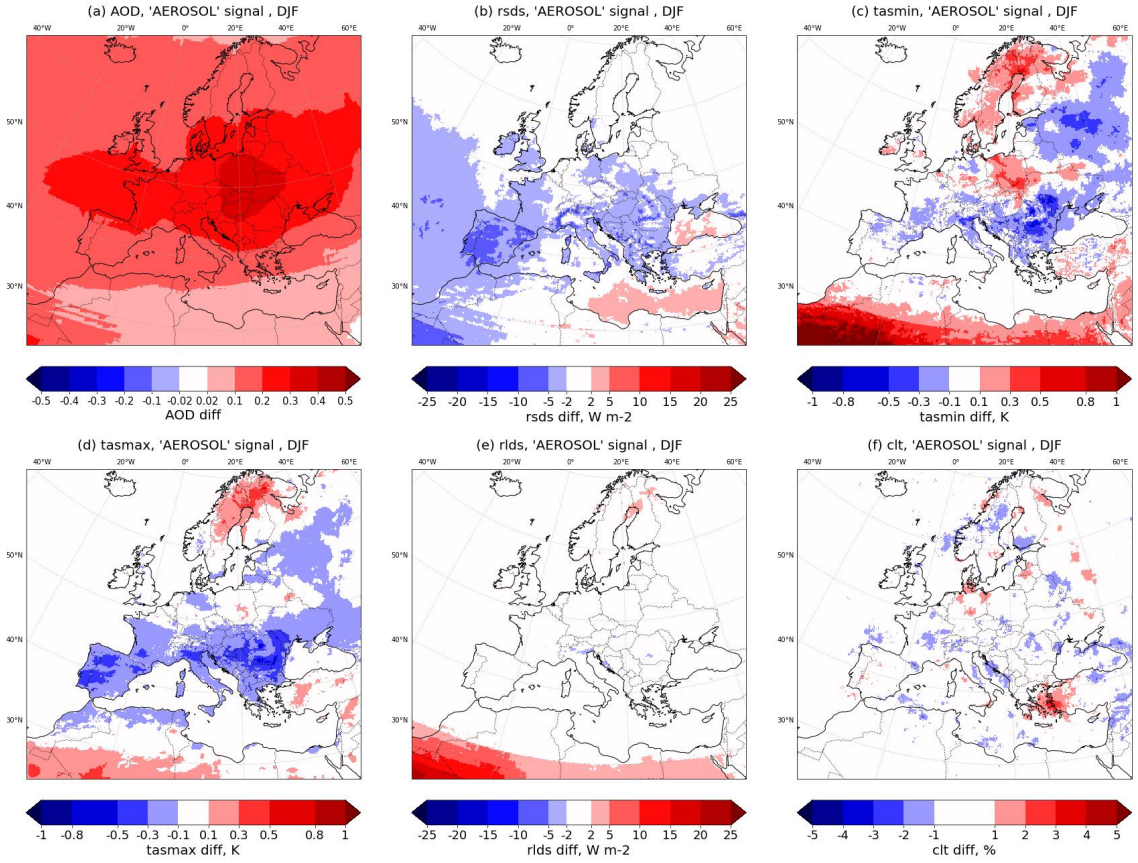

Figure S4. Mean differences (DJF 1980–1984) of Aerosol Optical Depth **AOD** (a), **rsds** (b), **tasmin** (c), **tasmax** (d), **rlds** (e) and **clt** (f) for the test with transient aerosol data (MACv2-SP, `C2I105`) minus the reference with Tegen aerosols (`C2I101`), cf. Table C1.

S2 Parameters of Planetary Boundary Layer Physics

`itype_z0` (test:3, reference:2)

Figure 8 shows seasonal mean differences for **tas**, **pr_amount**, and **ws** in DJF and JJA 1980–1984 exhibiting the impact of subgrid-scale orography contribution to surface roughness data. Additionally, Fig. S4 shows the mean difference in quantities directly related (turbulent fluxes **hlfs**, **hfss**) or showing a high sensitivity like mean sea level pressure **psl**.

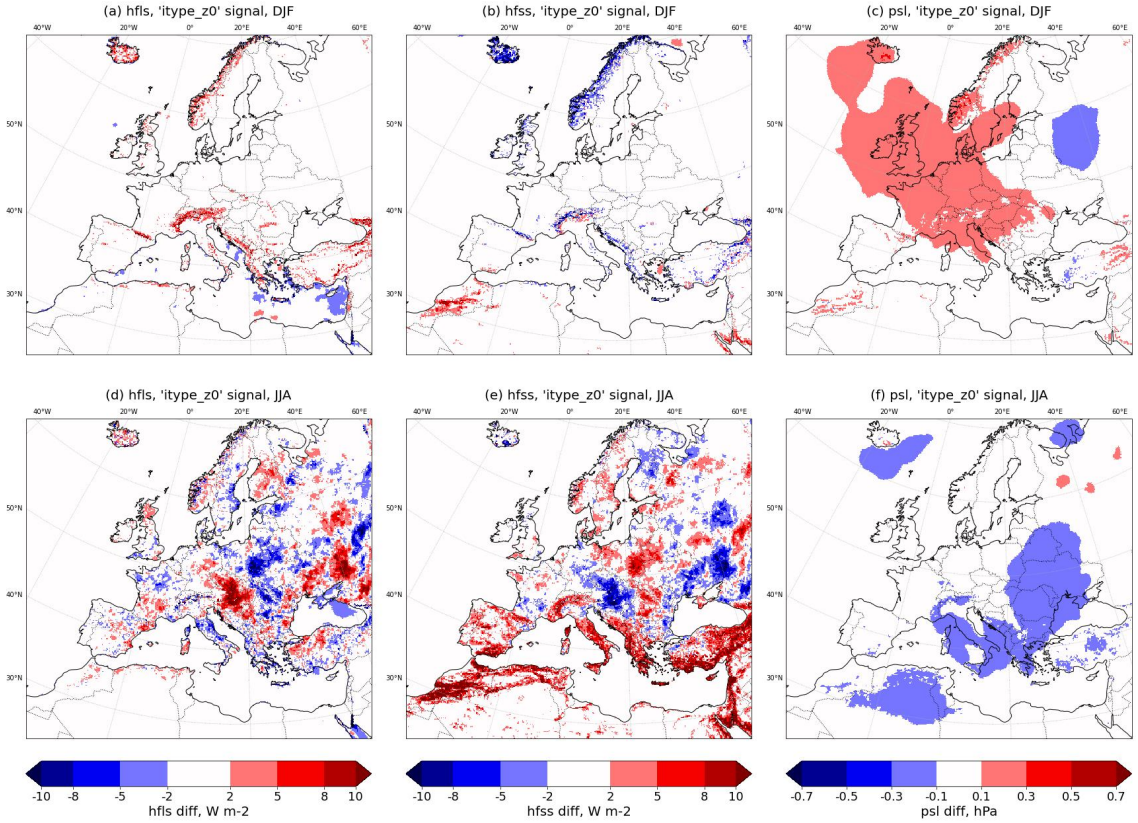

Figure S5. Mean DJF (top) and JJA (bottom) 1980–1984 differences for the change in type of roughness length data `itype_z0` and **hlfs** (left), **hfss** (center) and **psl** (right).

`rlam_heat` (test: 6.25, reference: 10)

Figure 9 shows seasonal mean differences for **hfls** in DJF and JJA 1980–1984 exhibiting the impact of reduced resistance to turbulent heat fluxes. Additionally, Fig. S6 shows the results for **tas**, **pr_amount** and **rlds**.

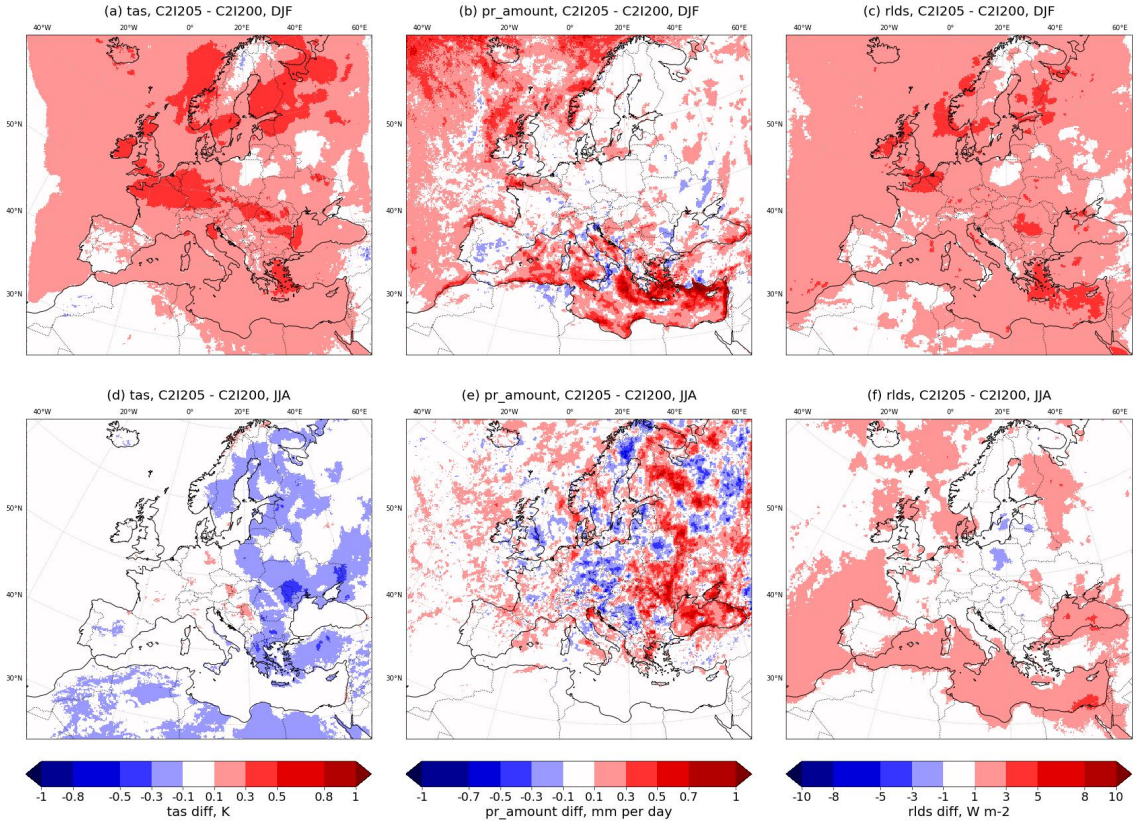

Figure S6. As Fig. S5 but for reduced minimum resistance to turbulent heat fluxes `rlam_heat` (10 (reference), 6.25 (test)) and **tas** (left), **pr_amount** (center) and **rlds** (right).

`rat_sea` (test: 0.4, reference: 0.7)

Figure 9 shows seasonal mean differences for **hfls** in DJF and JJA 1980–1984 exhibiting the impact of reduced resistance to turbulent heat fluxes. Additionally, Fig. S7 shows results for **tas**, **pr_amount** and **rlds**.

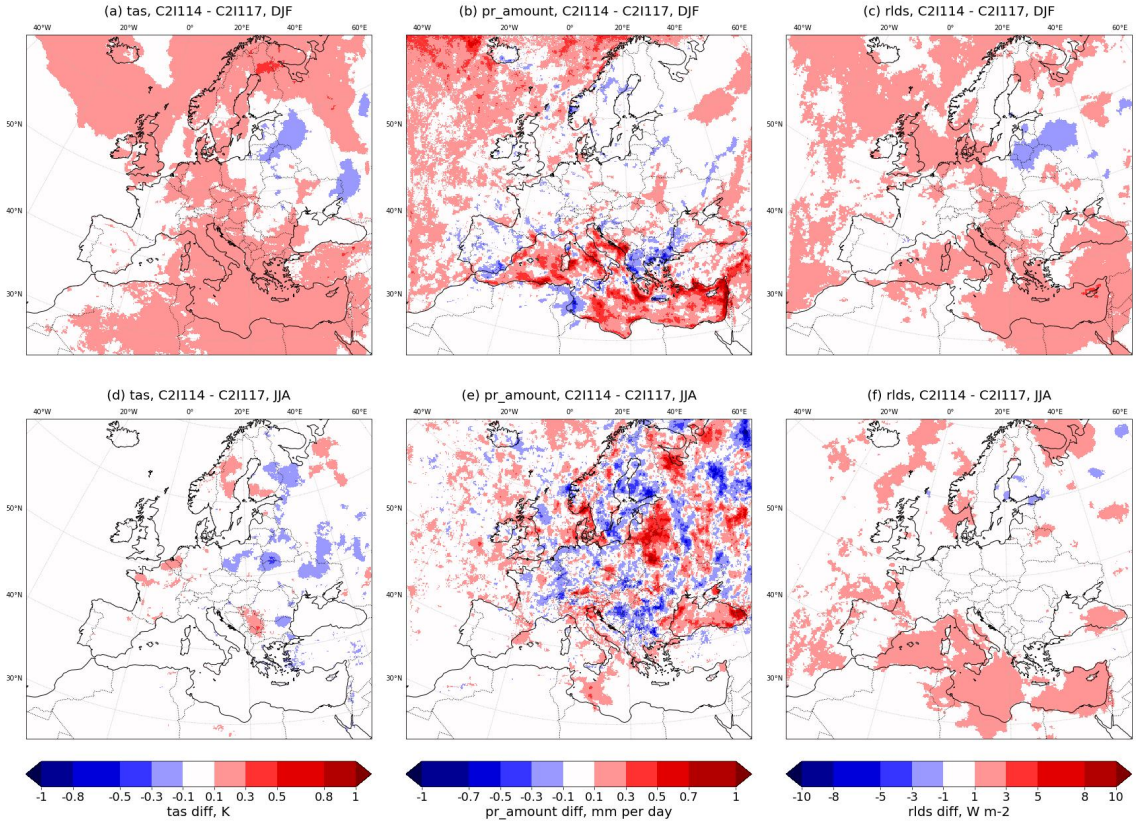

Figure S7. As Fig. S6 but for 2003–2008 and increased resistance to turbulent heat fluxes over water `rat_sea`.

`tune_albedo_wso(1)` (test: 0.1, reference: 0.0)

Figure 10 shows seasonal mean differences for **tasmin**, **tasmax** and **rsus** in DJF and JJA 2003–2008 exhibiting the impact of increased albedo at dry soil conditions. Additionally, Fig. S8 shows **tas**, **pr_amount** and **hfls**.

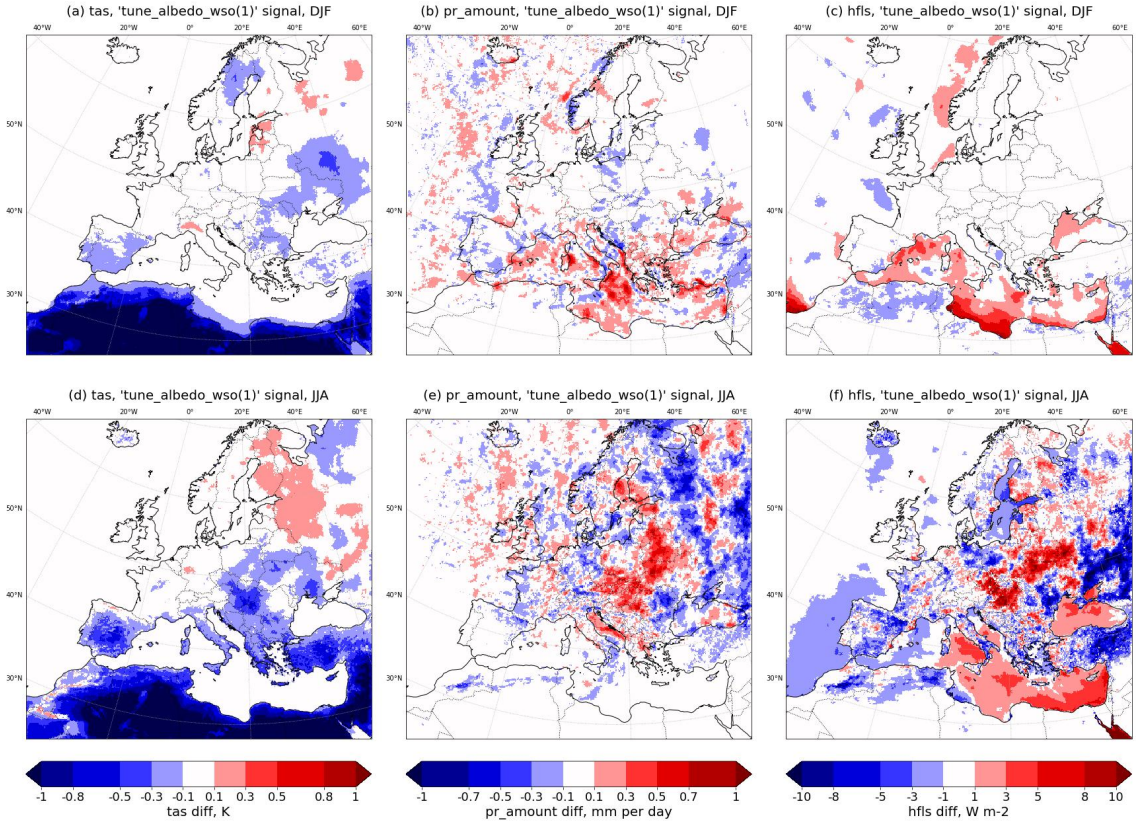

Figure S8. As Fig. S7 but for increased albedo for dry soils near surface `tune_albedo_wso(1)` and latent heat flux at the surface **hfls** (right).

`itype_hydmod` (test: 1, reference: 0)

Figure S9 shows seasonal mean differences for **tas**, **pr_amount** and **hfls** in DJF and JJA 1980–1984 exhibiting the impact of the parameterisation of horizontal soil water transport due to gravitation.

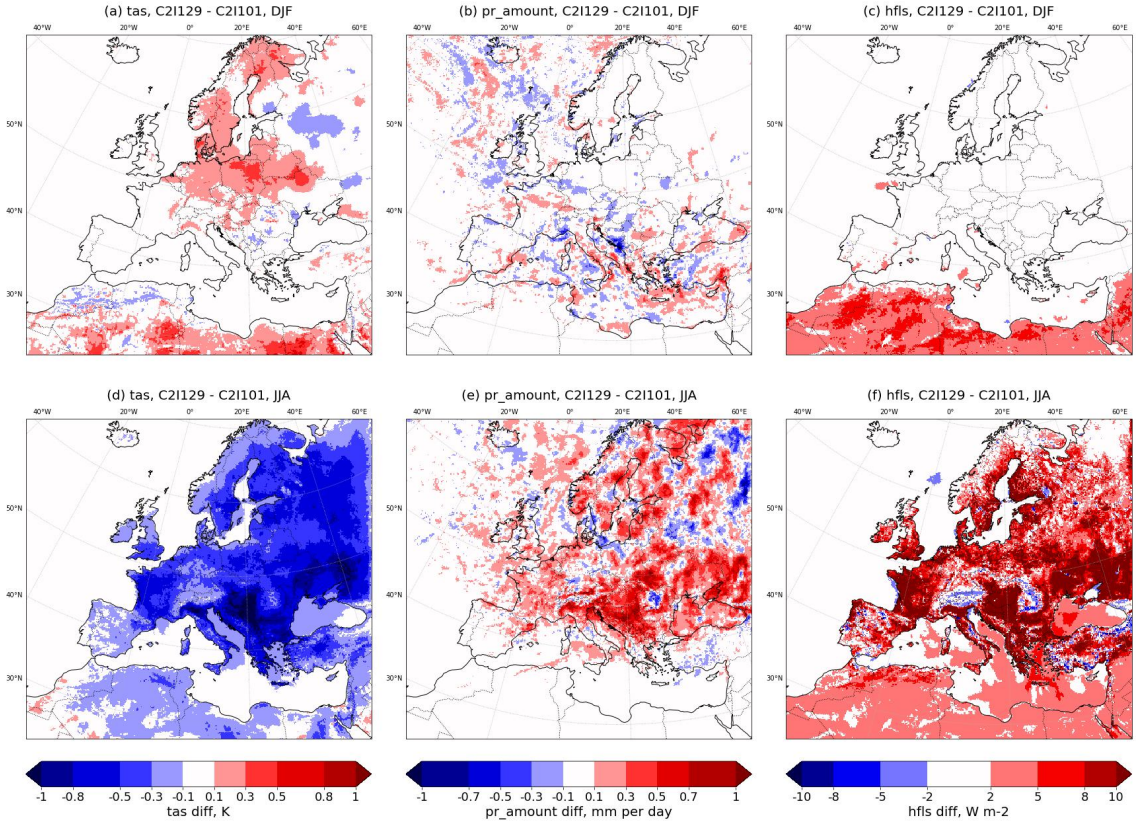

Figure S9. As Fig. S6 but for the impact of horizontal soil water transport due to gravitation (`itype_hydmod`) and **tas**, **pr_amount** and **hfls**.

S3 Parameters of PBL, mixing and convection related processes

`DTPHY` (test: dt2*, reference: dt1*)

Figure S10 shows seasonal mean differences for **tas**, **pr_amount** and **hfls** in DJF and JJA 1980–1984 exhibiting the impact of the parameterisation of horizontal soil water transport due to gravitation.

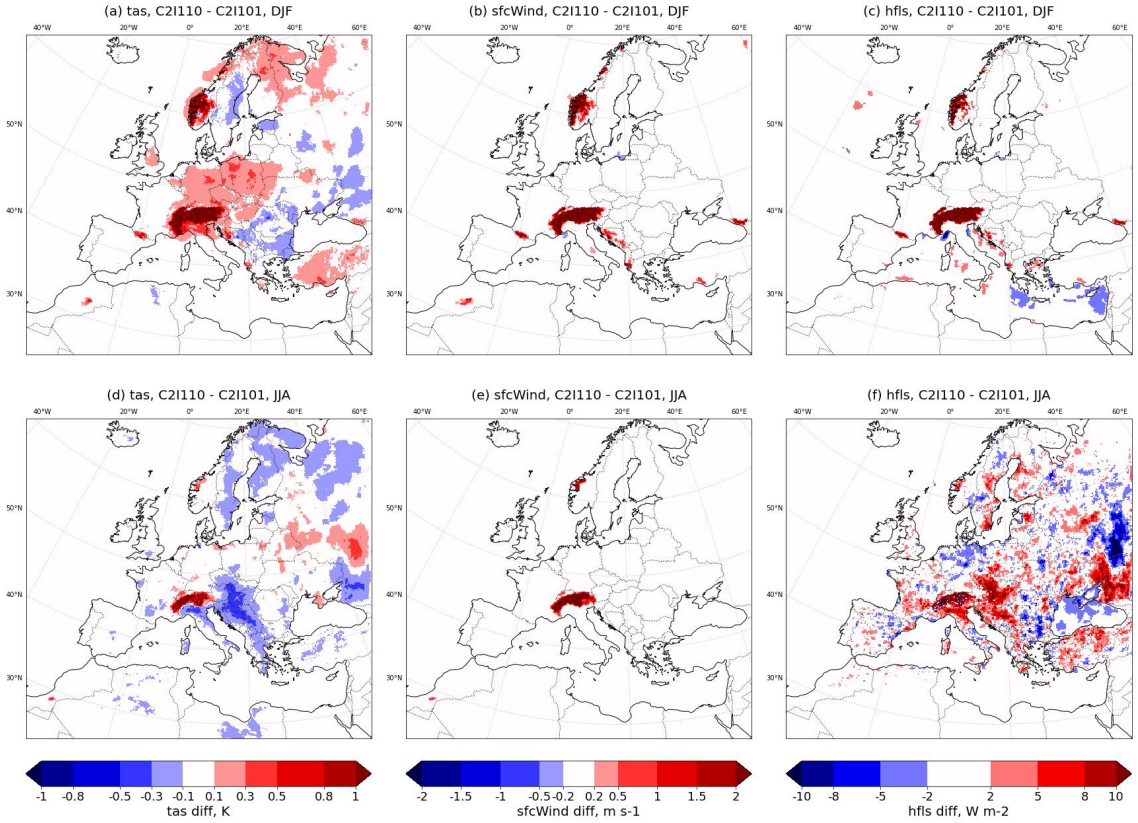

Figure S10. As Fig. S6 but for longer time increments between the calls of the parameterisations of convection, radiation, subgrid scale orography, and gravity wave drag `DTPHY` and **tas** (left), **sfcWind** (center) and **hfls** (right).

`tkhmin, tkmmin` (0.3,0.375) - (0.6,0.75)

Figure S11 shows seasonal mean differences for **tasmin**, **hfss** and **clt** in DJF and JJA 1980–1984 exhibiting the impact of reduction of the minimum vertical transport coefficient from (0.6,0.75) to (0.3, 0.375) for **tkhmin** and **tkmmin** respectively.

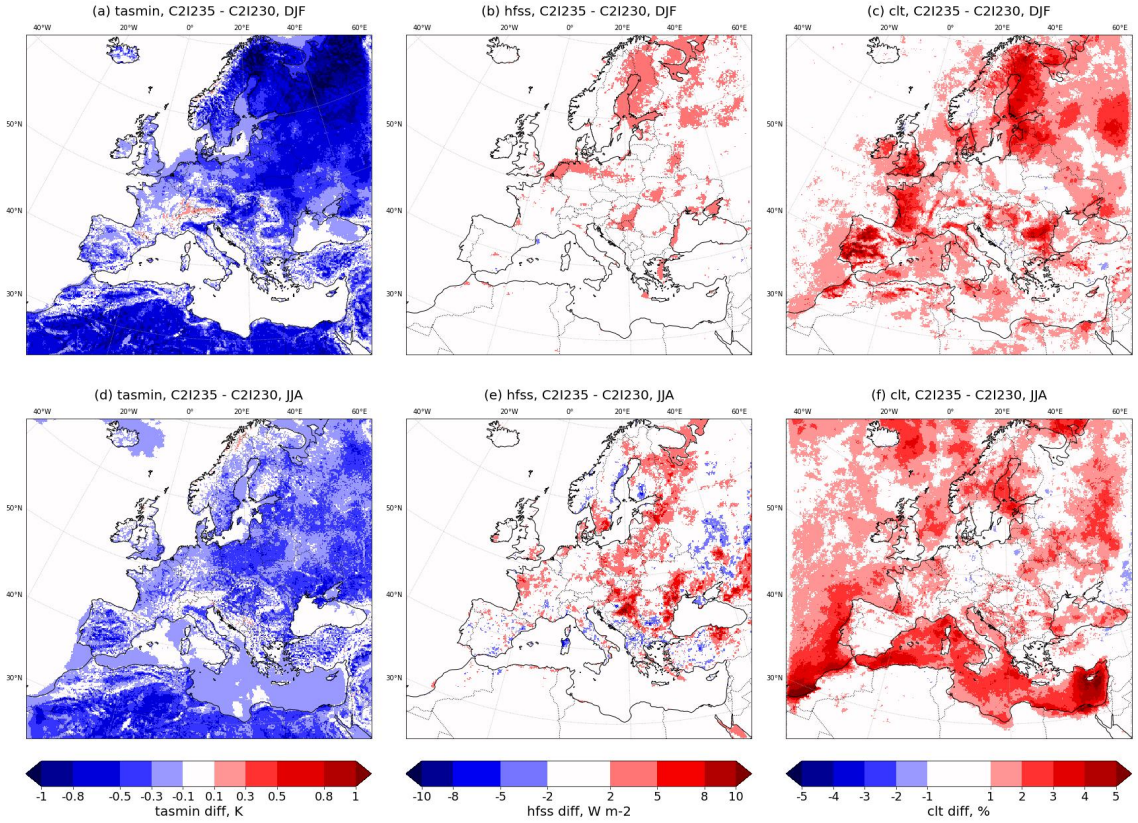

Figure S11. As Fig. S6 but for reduced minimum turbulent transport coefficients for heat `tkhmin` and momentum `tkmmin`, and **tasmin** (left), **hfss** (center) and **clt** (right).

S4 Parameters of Microphysics and Cloud diagnostic

Grid Scale Precipitation (GSCP) (test: 2-ice*, reference: 1-ice*)

Figure S12 shows seasonal mean differences for **tasmin**, **pr_amount** and **rsds** in DJF and JJA 1980–1984 exhibiting the impact of new ice-nucleation in the 1-moment microphysics scheme with two categories of ice, cloud ice and snow.

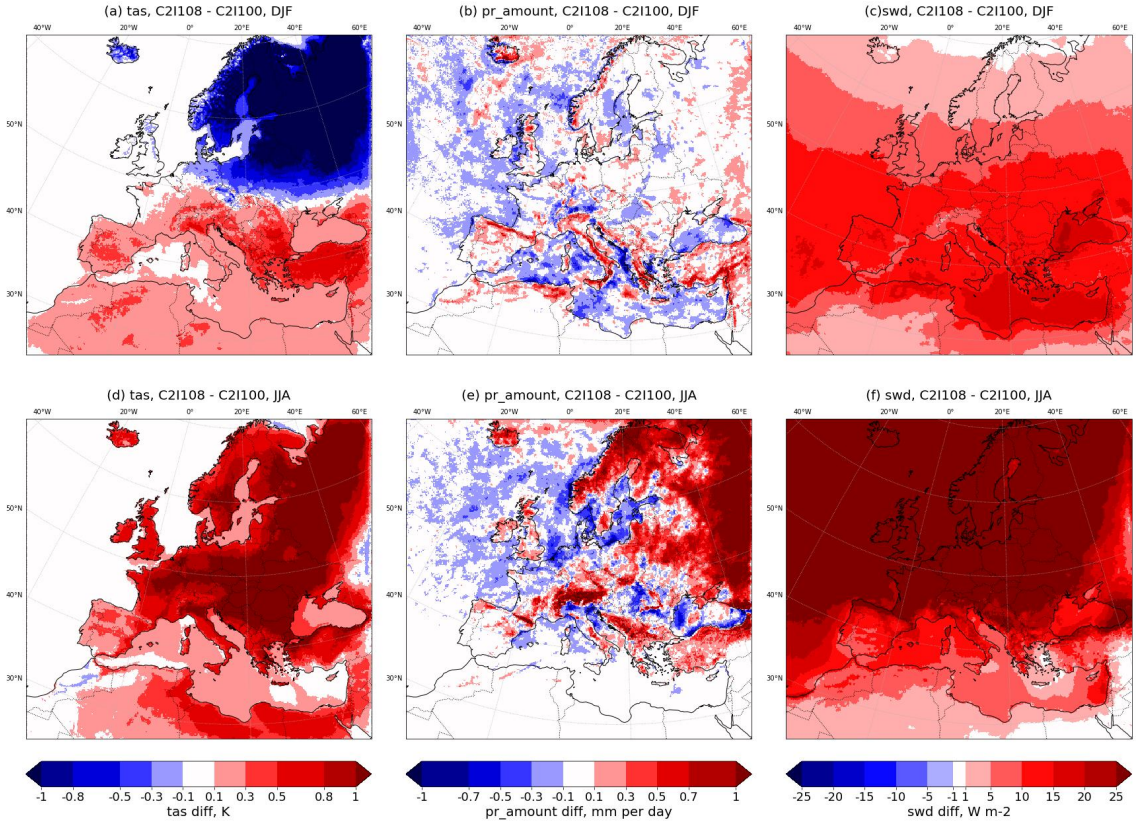

Figure S12. As Fig. S6 but for new ice nucleation in 1-moment microphysics scheme `inwp_gscp=3` and **tas** (left), **pr_amount** (center) and **rsds** (right).

`allow_overcast` (test: 0.9, reference: 1.0)

Figure 13 shows seasonal mean differences for **tas**, **pr_amount** and **clt** in DJF and JJA 1980–1984 exhibiting the impact of reduced shape factor of subgrid-scale cloud cover dependency on **rh**. Additionally, Fig. S13 shows the results for **tasmax** and the downward radiation components **rsds** and **rlds**.

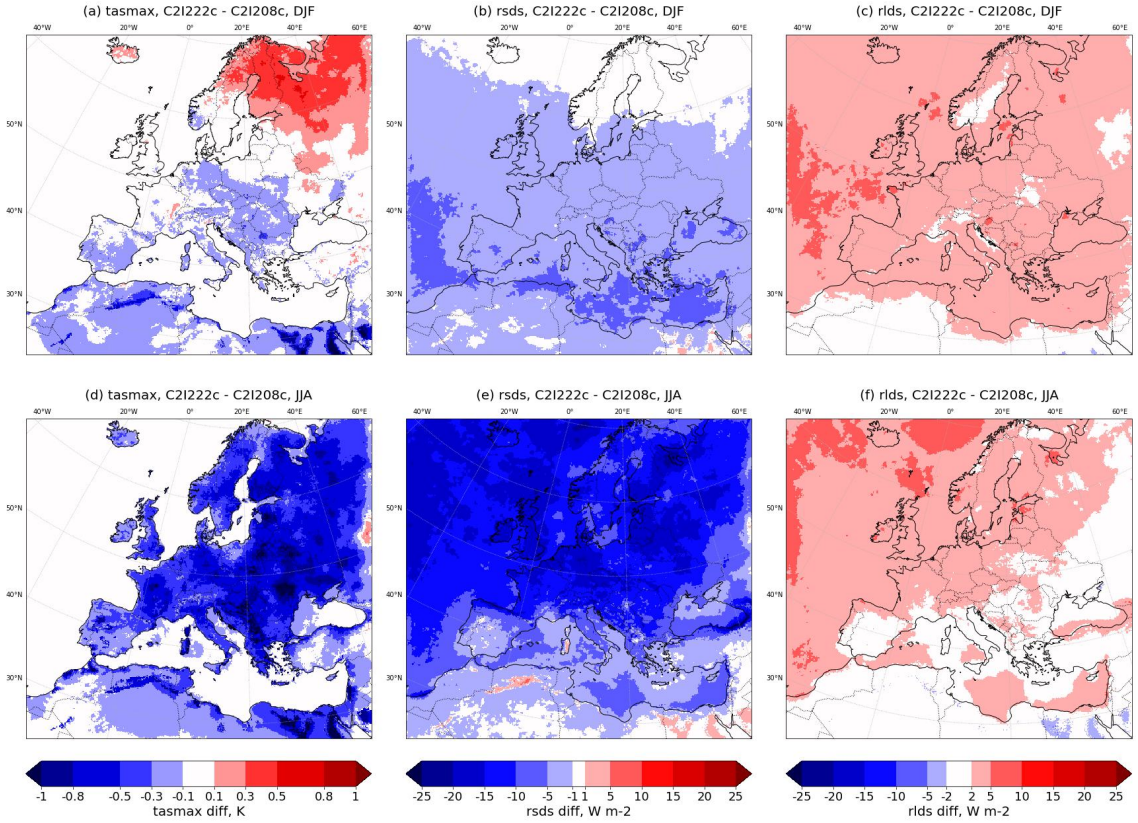

Figure S13. As Fig. 13 but for **tasmax** (left), **rsds** (center) and **rlds** (right).

`tune_box_liq` (test: 0.07, reference: 0.05)

Figure S14 shows seasonal mean differences for **tas**, **pr_amount**, and **clt** in JJA 1980–1984 exhibiting the impact of reduced shape factor of subgrid-scale cloud cover dependency on **rh**. Additionally, Fig. S13 shows the results for **tasmax** and the downward radiation components **rsds** and **rlds**.

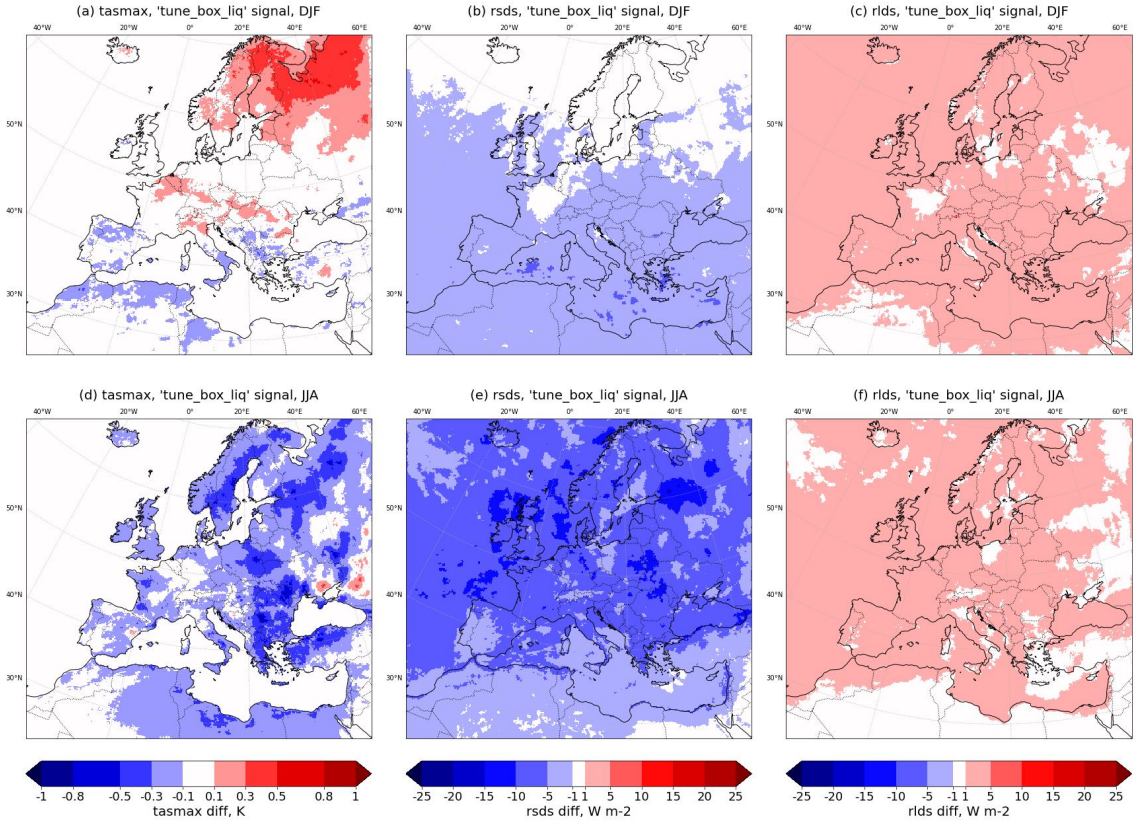

Figure S14. As Fig. S13 but for `tune_box_liq` for **tasmax** (left), **rsds** (center) and **rlds** (right).

`tune_box_liq_asy` (test: 4.0, reference: 3.25)

Figure 14 shows seasonal mean differences for **tas**, **pr_amount** and **clt** in JJA 1980–1984 exhibiting the impact of the scaling factor of asymmetry of the cloud cover for over- and undersaturation. Additionally, Fig. S15 shows the results for **tasmax** and the downward radiation components **rsds** and **rlds**.

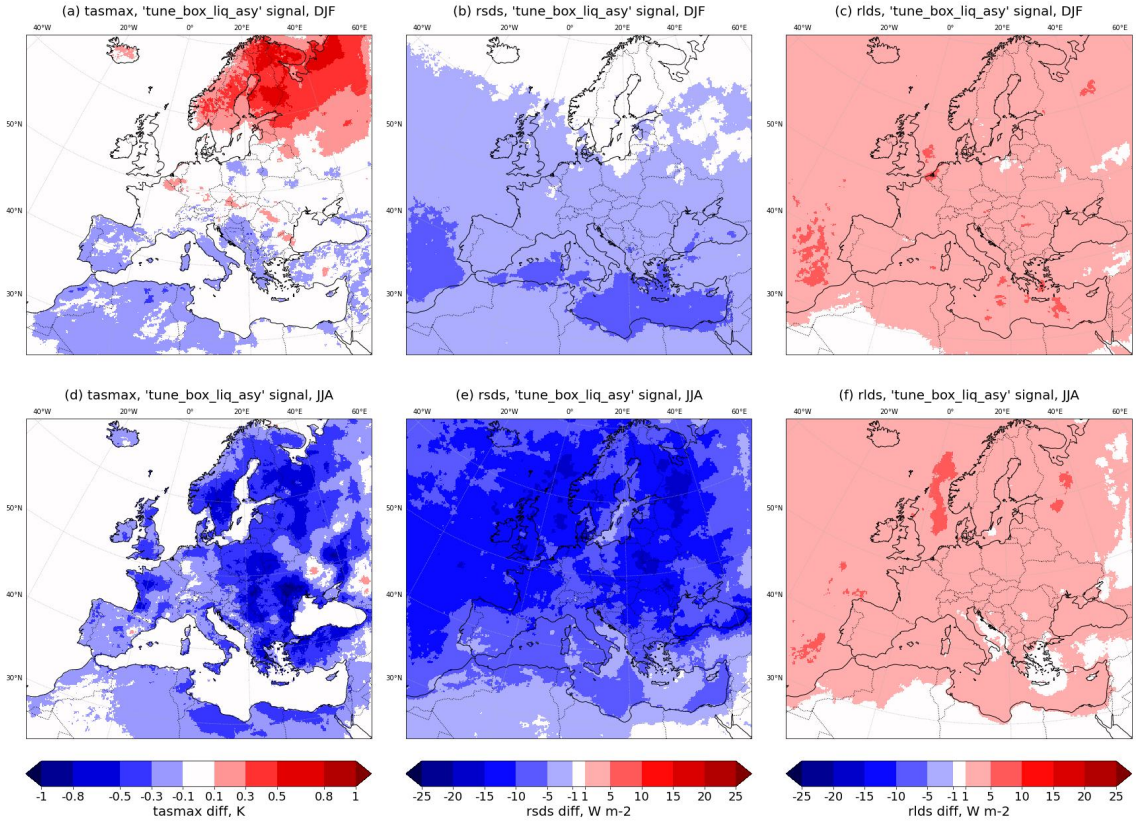

Figure S15. As Fig. S13 but for `tune_box_liq_asy`.

S5 Comprehensive evaluation results

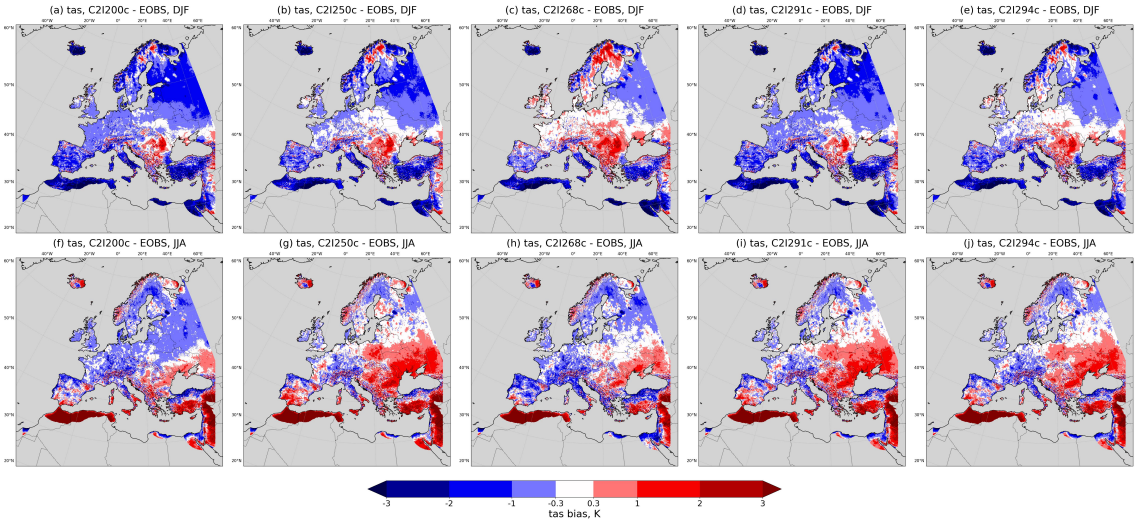

Figure S16. Seasonal mean differences in **tas** for winter (DJF) and summer (JJA) for the simulations considered in the final decision: C2I200c, C2I250c, C2I268c, C2I291c, and C2I294c to E-OBS version 29.0.

The seasonal mean biases of **tas** are compared in Fig. S16. We can draw the following conclusions: By comparing (a) to (b) and (f) to (g), it is clearly seen that the update of external datasets results in a positive shift of **tas** on the entire land surface. This results in the improvement of negative winter temperature bias, especially in Central Europe. This also holds for summer, however, `C2I250c` exhibits more pronounced positive biases over Eastern Europe; The negative winter bias of `C2I250c` over Central Europe (b) is further reduced by `C2I268c` (c) and `C2I294c` (e) configurations; The high positive summer bias of `C2I250c` over Eastern Europe (g) is reduced significantly by `C2I268c` (h) and slightly by `C2I291c` (i) and `C2I294c` (j) configurations; Overall, the `C2I291c` configuration has comparable quality to `C2I250c` – in summer, `C2I291c` is slightly worse (see b and d) and in winter slightly better (see i and g) than `C2I250c`.

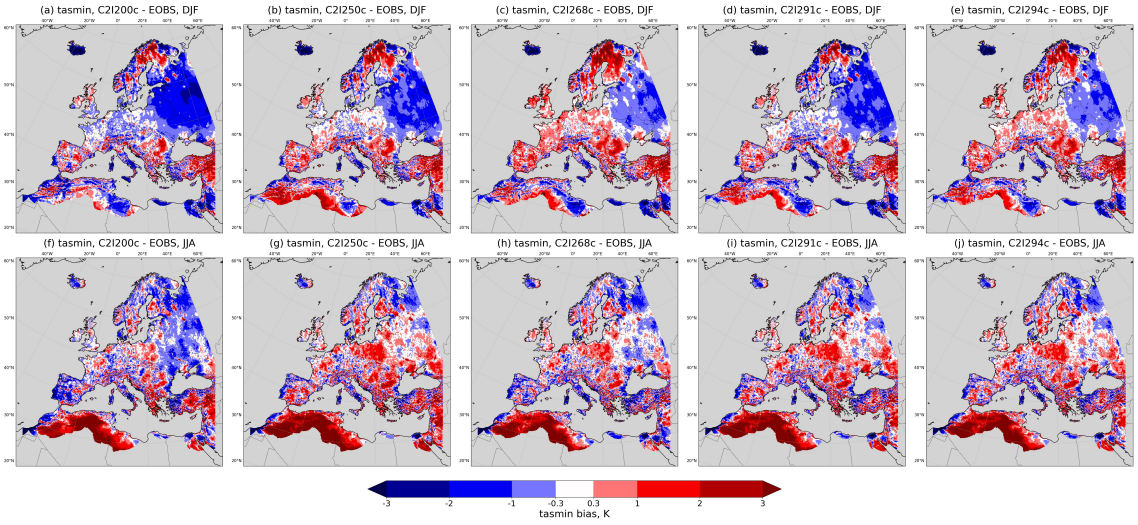

Figure S17. As Fig. S16 for seasonal mean differences in **tasmin**.

The seasonal mean biases of the daily **tasmin** are shown in Fig. S17. The outcomes are: As for daily mean **tas** in Fig. S16 we observe the positive shift for **tasmin** with updated external datasets by comparing (a) to (b) and (f) to (g). The winter negative bias is reduced; however, the summer positive bias became more pronounced over Central Europe; The optimized configurations `C2I268c`, `C2I291c`, `C2I294c` differ insignificantly to `C2I250c` for both seasons on the entire land surface (within 0.5 K).

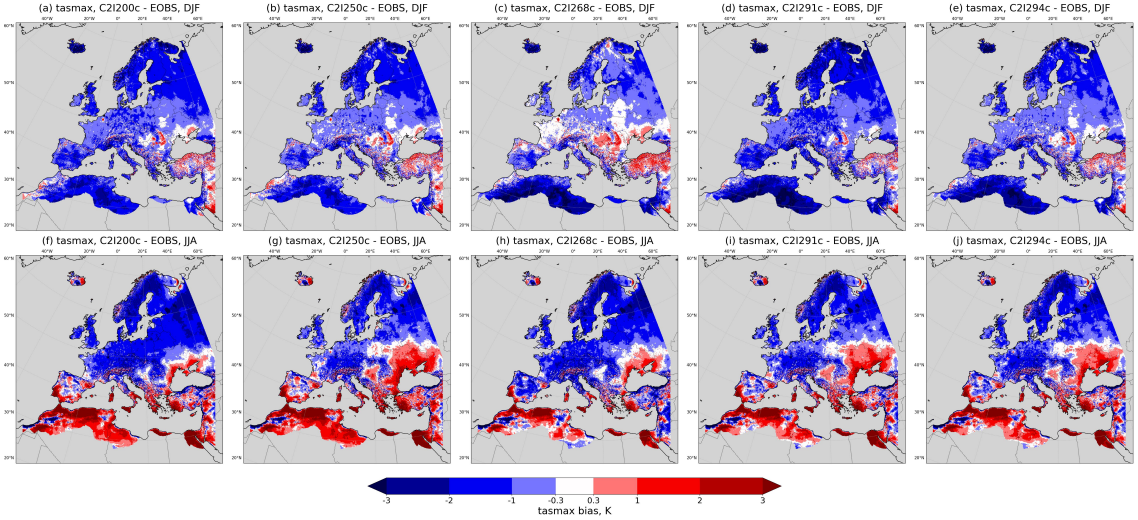

Figure S18. As Fig. S16 for seasonal mean differences in daily **tasmax**.

The seasonal mean biases of the daily maximum 2-meter temperature are shown in Fig. S18. The following can be stated: The same positive shift is observed for `C2I250c` compared to `C2I200c` that reduces the overall negative winter bias ((b) with respect to (a)). In a similar way the reduction of negative summer bias is obtained for Central Europe and positive summer bias is increased in Eastern Europe ((g) with respect to (f)). The negative winter bias is further reduced for `C2I268c` ((c) with respect to (b)). However, the negative summer bias is increased over Central Europe, while reducing the strong positive bias

over Eastern Europe ((h) with respect to (g)). The configuration C2I294c performs slightly better than C2I291c for both seasons.

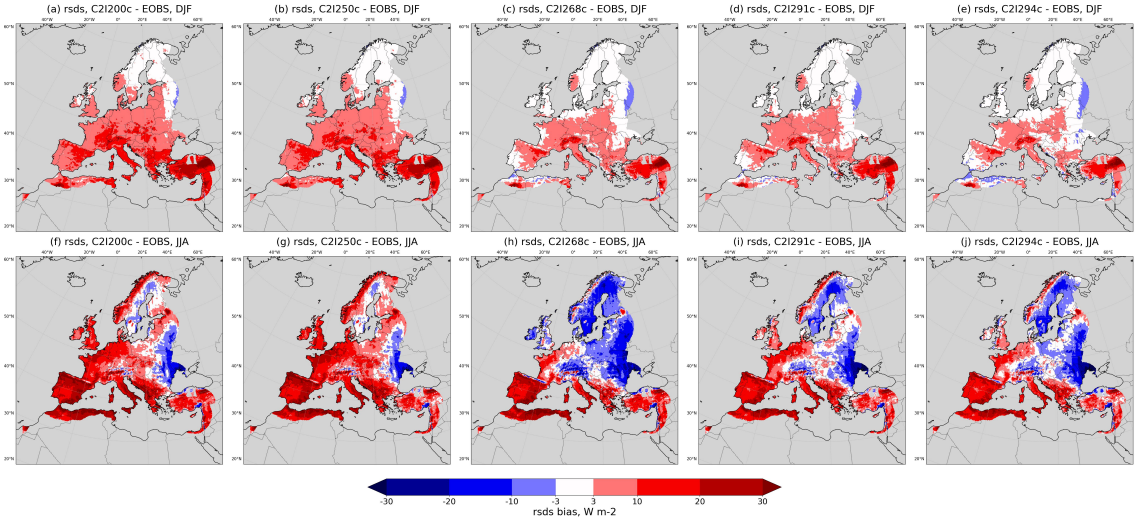

Figure S19. As Fig. S16 for seasonal mean differences in **rsds**.

The major improvements of model parameter optimisation are observed in **rsds**. That is shown in Fig. S19: Unlike for temperature variables, **rsds** shows no visible differences for C2I250c in comparison to C2I200c. For the winter season, C2I294c (e) shows the largest reduction of the positive bias with respect to C2I250c (b). The positive summer bias of C2I250c in Central Europe is significantly reduced in optimized configurations. The expert configuration C2I268c exhibits too large negative biases in East Europe (h), whereas LiMMo configurations are more balanced ((i) and (j)).

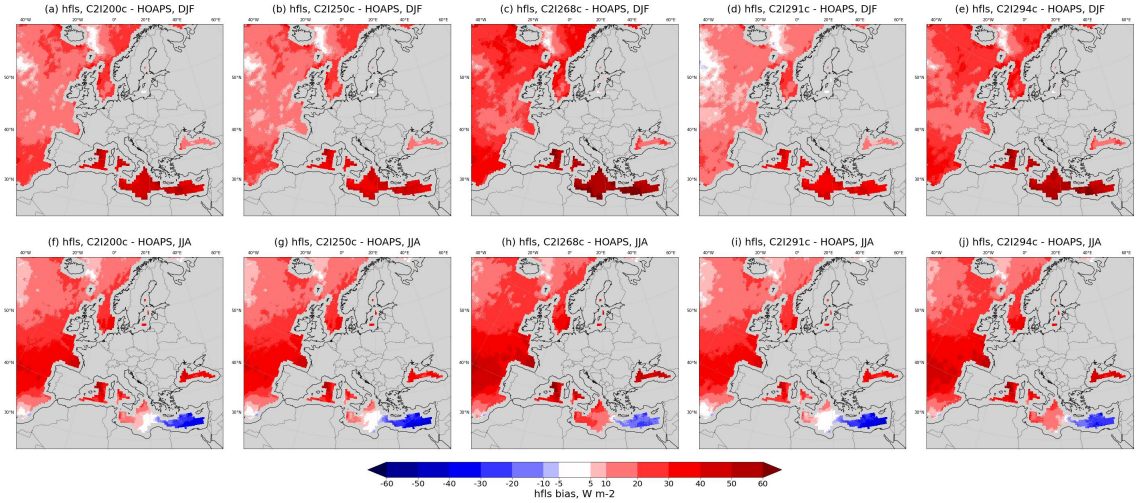

Figure S20. As Fig. S16 for seasonal mean differences of **hfls_o** in comparison to HOAPS.

Finally, we present the comparison of **hfls_o** against HOAPS in Fig. S20: The initial configuration C2I200c overall exhibits the overestimation of **hfls** over water, except the eastern part of the Mediterranean Sea in summer (f). The updated configuration C2I250c does not show significant changes on the **hfls_o** bias (see (b) and (g)). In contrast to this, the expert C2I268c and

LiMMo `C2I294c` configurations significantly increase overall positive bias of **hfls_o** in winter (see (c) and (e) relative to (b)). In summer, positive biases increase for the southern part of the Atlantic Ocean and the western part of the Mediterranean Sea (see (h) and (j) relative to (g)). The LiMMo configuration `C2I291c` is able to reduce the overall positive bias in winter (compare (d) to (b)) as well as to slightly lower the summer biases (compare (i) to (g)). Overall, the west-east summer gradient over the Mediterranean Sea observed by HOAPS is not captured by ICON-CLM for **hfls**.

References

Christensen, J. H. and Christensen, O. B.: A summary of the PRUDENCE model projections of changes in European climate by the end of this century, Climatic Change, 81, 7–30, https://doi.org/10.1007/s10584-006-9210-7, 2007.